Materials Today Bio 28 (2024) 101166

Contents lists available at ScienceDirect

Materials Today Bio

journal homepage: www.journals.elsevier.com/materials-today-bio

# Real-time detection and resection of sentinel lymph node metastasis in breast cancer through a rare earth nanoprobe based NIR-IIb fluorescence imaging

Zuo Yang [1], Yu Ji [1], Qian Jia [**], Yanbin Feng, Renchuan Ji, Mingli Bai, Haohao Yan, Fang Sun, Ruili Zhang [***], Zhongliang Wang [*]

*Lab of Molecular Imaging and Translational Medicine (MITM), Engineering Research Center of Molecular & Neuro-imaging, Ministry of Education, School of Life Science and Technology, Xidian University, Xi'an, Shaanxi, 710126, People's Republic of China*

ARTICLE INFO

*Keywords:*
NIR-II fluorescence
Metastasis
Sentinel lymph nodes
Intraoperative imaging
Rare-earth nanoparticles

ABSTRACT

Sentinel lymph node (SLN) biopsy is a commonly employed procedure for the routine assessment of axillary involvement in patients with breast cancer. Nevertheless, conventional SLN mapping cannot reliably distinguish the presence and absence of metastatic disease. Additionally, the complex anatomical structures and lymphatic drainage patterns surrounding tumor sites pose challenges to the sensitivity of the near-infrared fluorescence imaging with subcutaneously injected probes. To identifying the SLN metastases, we developed a novel nanoprobe for *in vivo* fluorescence imaging within the second near-infrared (NIR-II) range. This nanoprobe utilizes rare-earth nanoparticles (RENPs) to emit bright fluorescence at 1525 nm and is conjugated with tumor-targeted hyaluronic acid (HA) to facilitate the detection of metastatic SLN. Upon intravenous administration, RENPs@HA effectively migrated to SLNs and selectively entered metastatic breast tumor cells through CD44-mediated endocytosis. The RENPs@HA nanoprobes exhibited rapid accumulation in metastatic inguinal lymph nodes in mouse model, displaying a 5.8-fold-stronger fluorescence intensity to that observed in normal SLNs. Consequently, these nanoprobes effectively differentiate metastatic SLNs from normal SLNs. Importantly, the probes accurately detected micrometastases. These findings underscore the potential of RENPs@HA for real-time visualization and screening of SLNs metastasis.

## 1. Introduction

Identification of sentinel lymph node (SLN) metastasis is crucial for accurate diagnosis, pathological grading, and staging of tumors in patients with metastatic breast cancer. This is because these cancer cells primarily spread through the first sentinel nodes in a chain of lymph nodes that drain the primary tumor site [1]. By determining the presence or absence of SLN metastasis, unnecessary lymph node dissection and postoperative complications can be reduced by 60 % [2]. Biopsy and intraoperative frozen sections are considered the gold standard for determining the lymph node status (non-metastatic or metastatic) [3]. However, a biopsy is a lengthy procedure that imposes additional stress, necessitating repeated surgeries and hospital stays [4]. Even worse, inherent limitations of intraoperative frozen sections led a low detecting metastases sensitivity range of 23.5%–70 %, particularly in micro-metastases measuring less than 1 mm [5]. Consequently, there is an urgent need for rapid and sensitive approaches to accurately identify SLN metastases during surgery.

SLN localization and targeted excision are commonly guided by the administration of an injectable dye, methylene blue, a nuclide tracer, [technetium $^{99}$m sulfur colloid ($^{99}$mTc), or a combination of these [6,7]. However, these tracers exhibit limited specificity and possess various shortcomings, including radiation hazards, rapid photobleaching, and low signal-to-noise ratio (SNR) [8]. Although newer tracers such as $^{99}$mTc-Rituximab and indocyanine green (ICG)-Rituximab have demonstrated improved targeting of lymph nodes (LN), all the

* Corresponding author.
** Corresponding author.
*** Corresponding author.
*E-mail addresses:* jiaqian@xidian.edu.cn (Q. Jia), rlzhang@xidian.edu.cn (R. Zhang), wangzl@xidian.edu.cn (Z. Wang).
[1] These authors contributed equally to this work and share first authorship.

https://doi.org/10.1016/j.mtbio.2024.101166
Received 1 July 2024; Received in revised form 23 July 2024; Accepted 27 July 2024
Available online 30 July 2024
2590-0064/© 2024 Published by Elsevier Ltd. This is an open access article under the CC BY-NC-ND license (http://creativecommons.org/licenses/by-nc-nd/4.0/).

aforementioned tracers serve solely as tools for SLN mapping and do not provide any indication of the presence of metastasis [9–11]. Furthermore, lymphatic drainage from the primary tumor site is often not systematic, as evidenced by the complex drainage patterns observed in the interval or ectopic nodal locations [12]. This poses a significant challenge to subcutaneous injection as it increases the risk of initially missing or misdiagnosing the tumor. Additionally, currently employed dyes that rely solely on the lymphatic drainage pathway exhibit low specificity and penetration [13]. Consequently, there is an urgent demand for a robust SLNs metastasis-detecting imaging probe that possesses superior tumor specificity, enhanced penetration depth, a high SNR, and is independent of lymphatic drainage.

Rare-earth nanoparticles (RENPs) exhibit promising characteristics as NIR-II fluorescence probes owing to their exceptional photostability and biocompatibility, thereby presenting potential applications in lymphatic diseases [14]. The utilization of light excitation and emission within the NIR-II range (1000–1700 nm) enables deep tissue penetration, facilitating the attainment of high spatial and temporal resolutions with a favorable signal-to-background ratio [15]. The elegantly modularized construction of RENPs, has been reported to exhibit exceptional photostability and narrow emission bandwidth [16]. Through the design of multilayer nanostructures, energy migration and photon transition within these nanoparticles can be precisely controlled [17]. Consequently, our aim was to develop an RENP-based lymphatic tracer capable of efficiently metastasis targeting with enhanced penetration and improved affinity towards malignant cells. This tracer aids in the identification of the lymph node status.

The development of NIR-II fluorescent probes through conjugation of high-affinity ligands to overexpressed receptors has been established as an effective strategy for enhancing the accumulation of contrast agents in malignant lesions. In breast cancer, the overexpression of the CD44 receptor is a promising target for specific binding [18]. In this study, cerium-doped RENPs with an emission wavelength of 1525 nm in the NIR-IIb region were synthesized using fluorescence sensitization. For enhanced specificity, hyaluronic acid (HA), a ligand specific to CD44, was grafted onto the surface of the RENPs to form a novel probe named RENPs@HA. The nanoprobe demonstrated a strong affinity for lymphatic tissue and effectively detected primary tumors, lymph nodes metastases, and minute (<1 mm) disseminated peritoneal metastases (with SNRs exceeding 5) in both orthotopic tumor and advanced cancer models (as illustrated in Scheme 1). Using NIR-II fluorescence imaging guidance, we successfully achieved precise intraoperative detection of metastatic lymph nodes and complete resection of metastatic sentinel lymph nodes and tumors in mice. This study enhanced the clinical translational potential of NIR-II fluorescence image-guided SLN metastases screening and surgery, thereby improving cancer prognosis.

## 2. Experimental section

### 2.1. Materials and characterization

All chemical reagents, if not specified, were purchased from Sigma-Aldrich and used without purification. Yttrium oxide ($Y_2O_3$, 99.9 %), ytterbium oxide ($Yb_2O_3$, 99.9 %), erbium oxide ($Er_2O_3$, 99.9 %), neodymium oxide ($Nd_2O_3$, 99.9 %) and Cerium (III) carbonate hydrate ($Ce_2C_3O_9{\cdot}xH_2O$, 99.9 %) were purchased from Alfa Aesar. Trifluoroacetic acid ($C_2HF_3O_2$, 99 %) and Cyclohexane (99.5 %) were purchased from Innochem Co., Ltd. Indocyanine Green for Injection was purchased from Dandong Yichuang Pharmaceutical Co., Ltd. Unless otherwise noted, cell culture reagents were purchased from Invitrogen-GIBCO.

NIR-II living images were performed on Series II 900/1700-H NIR-II small animal imaging system made by Suzhou NIR-Optics Technology Co., Ltd. NIR-II fluorescence spectroscopy was detected by FLS 1000 steady-state and transient fluorescence spectrometer (Edinburgh Instruments Ltd., the UK). Ultraviolet–visible spectroscopy (UV–Vis) was recorded using a UV-2700i spectrophotometer (Shimadzu, Japan). Dynamic light scattering (DLS) and Zeta potential were determined through Malvern Zetasizer Nano ZS90. Living images of mice were performed on in-vivo imaging system (IVIS)-Lumia III spectrum (PerkinElmer, the US).

### 2.2. Synthesis of RENPs

**Trifluoroacetate salt of rare earth preparation:** Near-infrared II (NIR-II) rare earth particles were synthesized using the thermal decomposition method of trifluoroacetate salts. 5 g of yttrium oxide was added to a mixture of 10 mL deionized water and 5 mL trifluoroacetic acid. The mixture was then stirred at 95 °C for 12 h until the reactants became transparent. The insoluble impurities were removed by centrifugation at 8000 rpm. Ytterbium trifluoroacetate crystals were gradually obtained after dried overnight at 50 °C. Neodymium trifluoroacetate and lutetium trifluoroacetate were prepared according to the method above.

**Synthesis of the $NaYbF_4$:Er/Ce core of RENPs:** Trifluoroacetate erbium (0.02 mmol), trifluoroacetate cerium (0.1 mmol), trifluoroacetate ytterbium (0.89 mmol), trifluoroacetate sodium (1 mmol),

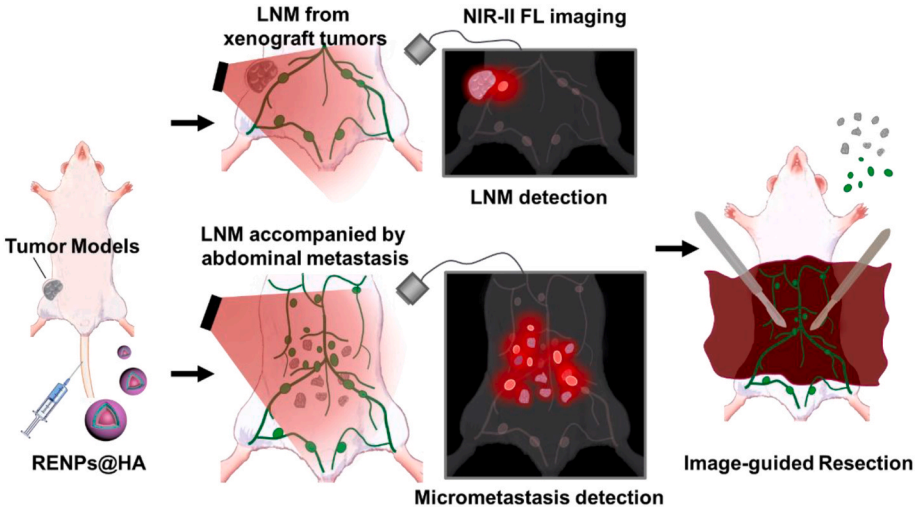


**Scheme 1.** Schematic illustration of NIR-II fluorescence image-guided lymph nodes metastases (LNM) screening and surgery. RENPs@HA are intravenously injected and accumulated in tumors and LNM. Upon 808 nm laser irradiation, NIR-II fluorescence imaging show precise intraoperative detection of LNM and micrometastasis in mouse model, which further guided the complete resection of metastatic SLNs and tumors in mice.

oleic acid (10 mmol), octadecene (20 mmol), oleyl amine (10 mmol) were sequentially into a sealed flask. Under argon protection, the mixture was slowly heated to 120 °C and maintain the temperature for 30 min. Once water evaporate, the mixture was heated to 300 °C and reacted for another 1 h. After cooling to room temperature, $NaYbF_4$:Er/Ce core of RENPs was collected by centrifuge at 5000 rpm after sufficient ethanol precipitation.

**Synthesis of the core shell structure of RENPs:** The $NaYbF_4$:Er/Ce core was mixed with trifluoroacetate sodium (0.5 mmol), trifluoroacetate ytterbium (0.5 mmol), oleic acid (20 mmol) and octadecene (20 mmol). In accordance with the previous step, heat the mixture to 305 °C and react for another 75 min to obtain $NaYbF_4$:Er/Ce@$NaYbF_4$. Then, $NaYbF_4$:/Er/Ce@$NaYF_4$Yb@$NaNdF_4$Yb was synthesized as the method above with additional neodymium trifluoroacetate. The $NaYbF_4$:/Er/Ce@$NaYF_4$Yb@$NaNdF_4$Yb@$NaLuF_4$ was synthesized with additional lutetium trifluoroacetate.

### 2.3. Surface functionalization of RENPs

40 mg of poly (1-octadecene maleic anhydride) (PMH) was dissolved in 10 mL of chloroform, the RENPs was then dropwise added into solution and stir for 18 h. After rotary evaporation and vacuum dry, 10 mL deionized water and 40 mg of 4-dimethylaminopyridine (DMAP) was added into the mixture with continued ultrasonic until the solution becomes transparent. The hydrophilic nanometer particle RENPs@PMH-COOH was subsequently obtained after centrifuge at 14000 rpm. 10 mg of $mPEG_{2000}$-$NH_2$ and 10 mg of 1-(3-dimethylaminopropyl)-3-ethyl carbodiimide hydrochloride (EDC) was mixed with RENPs@PMH-COOH and dissolved in 5 mL of MES (pH = 8.5) buffer solution. After EDC/NHS reaction, 20 mg HA (MW = 8600) were added into the obtained RENPs@PEG solution, the factionalized RENPs@HA was finally harvested by ultrafiltration3 h later.

### 2.4. Determination of the RENPs@HA photostability

ICG solution (50 μg $mL^{-1}$) and RENPs@HA (100 μg $mL^{-1}$) were exposed under an 808 nm laser (300 mW $cm^{-2}$) irradiation. Imaging was performed with the exposure time of 100 ms at different laser irradiation time points. To optimize the signal collection conditions, 1500 nm and 1000 nm long-pass filters (LP 1500 and LP 1000) were selected to acquire NIR-IIb imaging of RENPs@HA and ICG through a home-built InGaAs setup.

### 2.5. Cell cultures

Human breast cancer cell line MCF-7 and MDA-MB-231, human mammary epithelial cell line MCF-10A and mouse breast cancer cell line 4T1 were maintained in RPMI-1640 medium (C11875093BT, Gibco) with 10 % fetal bovine serum (FBS; 10091148, Gibco, USA), 1 % penicillin/streptomycin (KGY0023, KeyGEN BioTECH), and passaged every other day.

### 2.6. Animals

All animals used in this study were bred and housed under specific pathogen-free conditions at the Fourth Military Medical University. Mice were housed in a regulated environment (22 ± 2 °C, 55 ± 5 % humidity, and 12:12-h light: dark cycle with lights on at 8:00 a.m.) and received a standard diet. Food and water were accessible ad libitum. All procedures on mice were followed National Institutes of Health guidelines for care of animals. All applicable institutional guidelines for the care and use of animals were followed. Female BALB/c nude mice (5–6 weeks) were obtained from Fourth Military Medical University. To establish the 4T1 tumor xenograft model, $1 \times 10^6$ murine breast cancer 4T1-Luc cells were subcutaneously injected to the right lower limb of each mouse. For the abdominal cavity metastatic model, $2 \times 10^5$ 4T1-Luc cells were intraperitoneally injected into the mice. Animal protocols related to this study were reviewed and approved by the Institutional Animal Care and Use Committee of the Fourth Military Medical University (approval number: 20220312).

### 2.7. Fluorescence imaging of the mice

The BALB/c nude mice were intravenously injected with 100 μL RENPs@HA probes (0.5 mg $mL^{-1}$). Fluorescence images were acquired by Series II 900/1700-H with a 640 × 512 pixel InGaAs-NIRvana640LN camera. To optimize the signal collection conditions, LP 1500 and LP 1000 were selected to acquire imaging of the whole-body vasculature and intact local microvascular.

### 2.8. Imaging and surgical resection of abdominal metastases

The mice with abdominal metastasis were injected with the RENPs@HA probes (100 μL, 0.2 mg $mL^{-1}$). Perform intraoperative imaging 1 h later. Anesthetize the mice, fix their limbs, use surgical scissors to cut open the abdominal skin, and near-infrared fluorescence imaging was performed 1h post injection. Subsequently, the lesions were surgically removed under the guidance of NIR-IIb imaging.

### 2.9. Statistical analysis

Data values are expressed as the mean ± standard deviation (SD), and the analysis of all data was limited to analysis of two tailed Student's t-test. *: $P < 0.05$ was considered statistically significant. **: $P < 0.01$ and ***: $P < 0.001$ was considered highly statistically significant.

## 3. Results and discussion

### 3.1. Characterization of RENPs@HA

Using a $Ce^{3+}$ doped strategy to enhance the nanoparticle core down-conversion pathway and suppress upconversion, we synthesized core-shell $NaYF_4$:Yb/Er/Ce@$NaYF_4$:Yb@$NaNdF_4$:Yb@$NaLuF_4$ Er-RENPs (referred to hereafter as RENPs) with NIR-IIb emission at approximately 1550 nm using a layer-by-layer epitaxial growth method [19]. Transmission electron microscopy (TEM) and dynamic light scattering (DLS) confirmed the merits of the RENPs in terms of uniform and suitable diameters of 25 nm, with good dispersibility (Fig. 1A and B). Nanoagents with hydrodynamic diameters of 10–50 nm is widely known for their rapid uptake into the lymphatic system, which effectively identifies the SLNs [20,21]. The prepared RENPs were transformed into water-stable state by PMH-PEG coating (RENPs@PMH-PEG), and then HA was covalently bound to the surfaces to form RENPs@HA via the EDC-NHS reaction. Successful conjugation of PEG and HA sequentially diminished the zeta potential of RENPs from 24.3 ± 1.2 mV to 4.4 ± 1.0 mV, and further −17.2 ± 2.4 mV (Fig. 1C). The dispersal and size uniformity of RENPs@HA were also proved by DLS and TEM results (Fig. 1A; Fig. SI 1A). Because of the HA coating, the probe remained stable without obvious changes in particle size upon dispersal in deionized water, physiological saline, or serum for at least three days (Fig. SI 2A).

Under 808 nm laser excitation, RENPs@HA exhibited strong NIR-IIb fluorescence, with the emission spectrum peaking at 1525 nm (Fig. 1D; Fig. SI 1B) and stable fluorescence intensity remained at least three days upon dispersal in various solution (Fig. SI 2B). For biological imaging, the optical stability of the RENPs@HA was tested under continuous laser irradiation for 30 min. Compared to the clinically approved NIR dye ICG, RENPs@HA was more optically stable (Fig. 1E and F). To further test the potential of imaging deeper tissues, fluorescence images of capillaries filled with RENPs@HA or ICG in solution was imaged with pork tissue slice covering and showed significant differences in penetration depth (7 mm vs. 3 mm) (Fig. 1G). Gaussian-fitted full width at

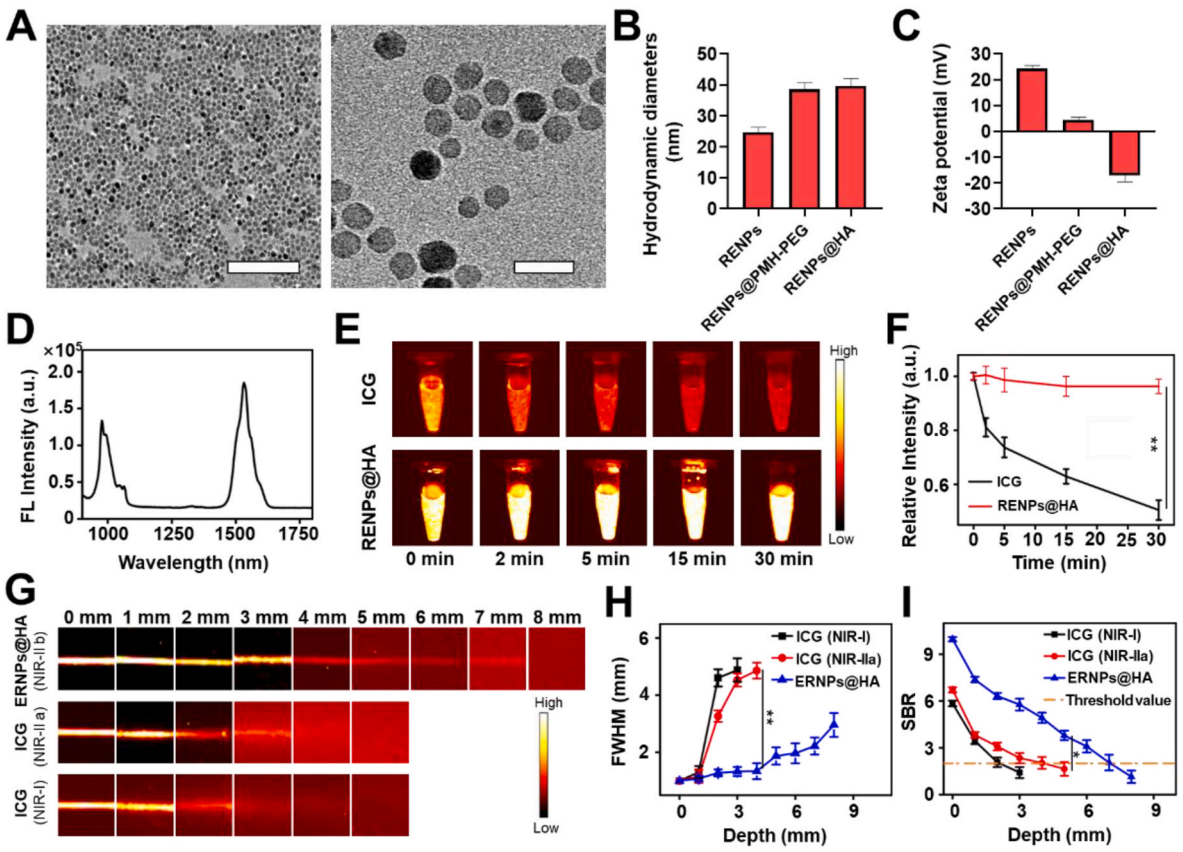


**Fig. 1.** Characterization of RENPs@HA. (**A**) TEM images of RENPs (left), scale bar 500 nm, and RENPs@HA (right), scale bar 50 nm. (**B**) Hydrodynamic diameter and (**C**) zeta potential of RENPs, RENPs@PMH-PEG and RENPs@HA. (**D**) Fluorescence intensity of RENPs@HA. (**E, F**) NIR fluorescence images of RENPs@HA (100 μg $mL^{-1}$) and ICG (50 μg $mL^{-1}$) in various biological media under irradiation at 808 nm with a power density of 15 W $cm^{-2}$. (**G**) NIR fluorescence images of phantom tissues showing complete attenuation of ICG by 3 mm in NIR-I or NIR-IIa regions, whereas signals of RENPs@HA persist through 7 mm (exposure time: 50 ms, power density: 15 W $cm^{-2}$, concentration of RENPs@HA: 100 μg $mL^{-1}$ and concentration of ICG: 50 μg $mL^{-1}$). (**H**) FWHM and (**I**) SBR of RENPs@HA and ICG based on the phantom tissue depth. Data are expressed as the mean ± SD (n = 3).

half maximum (FWHM) analysis showed decreased fluorescence intensity of RENPs@HA along with the increasing phantom depth, which gradually appeared after the thickness exceeded 5 mm because of the weakened scattering of photons (Fig. 1H and I).

To further confirm the high-resolution NIR-IIb imaging of RENPs@HA, fast-body vascular imaging of BALB/c nude mice was performed. Under 808-nm laser excitation after intervenors injection, mice clearly displayed whole-body vasculature imaging (Fig. 2A) and intact local microvasculature, including ear microvasculature, abdominal vasculature, brain microvasculature mesh, and tumor neovascularization (Fig. 2B–E). Additionally, microvascular cross-sections within the region of similar position and length were chosen (yellow line in figures), and the fluorescence signal was quantitatively analyzed by Gaussian fitting. The whole-body imaging results demonstrated high-sensitivity discrimination of brain microvasculature with a diameter of approximately 0.89 mm and superior vena cava vessels, the SNR of which was up to 9.45. (Fig. SI 3A–C). In addition, the ear vein microregion imaging showed observable microvessels with an FWHM of only 41 μm and excellent resolution (Fig. 2F, G, and I). Rather than only three microvessels observed in NIR-IIa brain microvascular imaging (Fig. SI 3D and E), NIR-IIb imaging of RENPs@HA clearly visualized six microvessels with an FWHM as low as 68 μm and accurately distinguished two vessels separated by 90 μm (Fig. 2H), indicating the outstanding sensitivity and resolution of RENPs@HA in NIR-IIb living imaging.

### 3.2. Targeting ability of RENPs@HA in CD44 high expression cells

The biosafety and targeting potential of RENPs@HA were evaluated *in vitro* as a feasibility study. MTT assays were performed on non-tumorigenic breast epithelial (MCF10A) and breast cancer (MCF-7 and MDA-MB-231) cells to evaluate the cytotoxicity of RENPs@HA. Cell viability results suggested no obvious cytotoxic effects of RENPs@HA (Fig. 3A–C). RENPs@HA concentration of 0.2 mg $mL^{-1}$, a quarter of no-observed-adverse-effect level (survival rate >95 %), was selected as the reference concentration used in the present study. Cellular uptake of RENPs@HA nanoprobes was investigated using confocal laser scanning microscopy (CLSM) and flow cytometry (FCM). Bright fluorescence was observed in MDA-MB-231 cells (high CD44 expression) rather than low CD44-expressed MCF-7 cells after 4 h of co-incubation with FITC dye-labeled NIR-II NPs, indicating that the CD44-HA mediated interaction of RENPs@HA (Fig. 3D). Flow cytometry results also supported this inference, that RENPs@HA were taken up by less than 1.4 % of MCF10A cells (Fig. 3E). These results indicated the potential of RENPs@HA for breast cancer-specific bioimaging.

### 3.3. In vivo and ex vivo biodistribution and biocompatibility of RENPs@HA

The *in vivo* behavior of RENPs@HA was investigated in healthy nude mice. NIR-IIb fluorescence signals were distinctly observed in systemic tissues within 1 h and decreased in 4 h post injection, indicating the rapid distribution of RENPs@HA (Fig. 4A). The liver emitted continuous detectable fluorescence signals with elimination latencies longer than

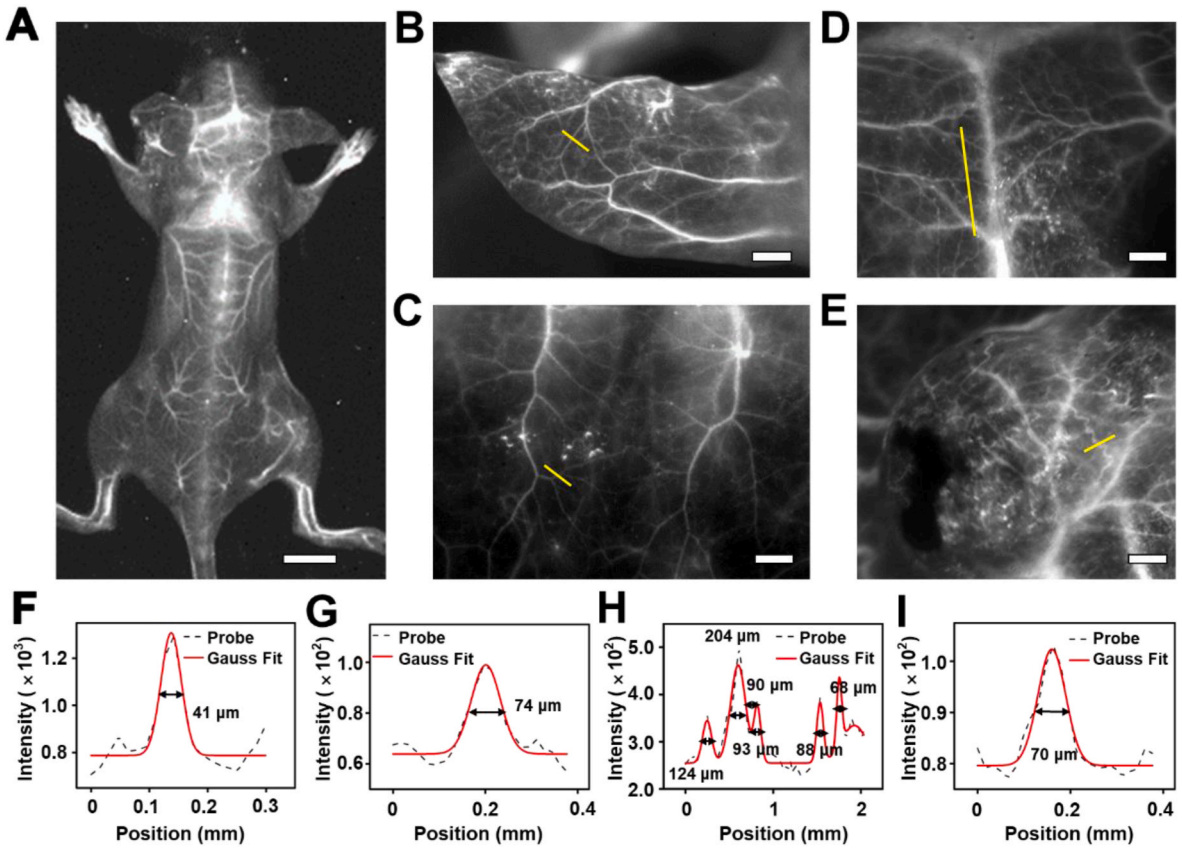


**Fig. 2.** NIR-IIb bioimaging of (**A**) whole-body (scale bar 10 mm), (**B**) ear (scale bar 2 mm), (**C**) abdomen (scale bar 2 mm), (**D**) brain (scale bar 0.5 mm), and (**E**) tumor (scale bar 1 mm) after intravenous injection of RENPs@HA (0.5 mg $mL^{-1}$, 100 μL). (**F–I**) Fluorescence intensity profiles (dashed black line) and Gaussian fitting curve (solid red line) along the yellow lines in the NIR-IIb fluorescence image shown in (**B–E**).

12 h in the ventral view, suggesting terminal elimination of RENPs@HA by the hepatobiliary systemand further guarantee the biological safety in living imaging. Although rapid elimination poses challenges to the imaging window, the enhanced fluorescence quantum yield of RENPs@HA in the NIR-IIb region by $Ce^{3+}$ doping and tumor-targeting HA functionalization should ensure tumor enrichment of the probes [22].

No significant weight differences or adverse events were observed in the RENPs@HA-exposed mice (Fig. 4B). Additionally, *ex vivo* imaging of the isolated organs indicated that the RENPs@HA NPs were mainly deposited in the liver, spleen, and lungs and eliminated in seven days (Fig. 4C). Although fluorescence signals showed retention of probes in spleen, serum biochemical analysis and hematoxylin and eosin (H&E)-stained tissue sections showed no overt long-term damage including inflammatory changes and threats to hematopoietic function (Fig. SI 4). Overall, RENPs@HA exhibited excellent optical performance, favorable clearance, and good biocompatibility *in vivo*, which promotes the translational capability of the nanoprobes in diverse biological applications.

### 3.4. *In vivo targeting of CD44-expressing breast tumors by RENPs@HA*

The applicability of RENPs@HA for intraoperative imaging was evaluated using a nude mouse model bearing MDA-MB-231 subcutaneous tumors. Mice with a volume of approximately 100 $mm^3$ were intravenously injected with 1 mg $kg^{-1}$ RENPs@HA, followed by imaging in dorsal view to avoid the mononuclear phagocyte system signal interference [23]. As shown in Fig. 4D, the SNR of tumor gradually increased over time and reached a maximum 10 h after probes injection. The rapid tumor-targeting accumulation of RENPs@HA may be attributed to its small size and HA modification, which facilitated the EPR effect [24]. To illustrate the specificity of tumor targeting, folic acid (FA)-coated RENPs (RENPs@FA) and unmodified RENPs@PEG were used as controls for tumor imaging [25]. The results showed that the tumor-to-background ratio of RENPs@HA maintained around 2.8–3.2 for at least 10 h (Fig. 4E), significantly higher than that of RENPs@FA (decrease from 2.2 to 1.0 within 6 h) or RENPs@PEG (decrease from 1.7 to 1.0 within 4 h), suggesting its higher specificity with CD44 expressing tumor.

### 3.5. *The timely diagnosis of LNs metastasis*

Given the high sensitivity and specificity of RENPs@HA living imaging, we further investigated the capability of the reported probe to detect LNs metastasis. LNs metastasis models were developed using 4T1-Luc tumors bearing mice in the right paw, and were imaged after footpad injection of the probe (1 mg $kg^{-1}$). To mimic clinical practice, we covered the paw region with a black sheet to better detect and demonstrate the signal during imaging. As shown in Fig. 5A, strong fluorescence signals were observed in the popliteal and sciatic LNs of the tumor-bearing mice. However, the fluorescence signals gradually spread from the popliteal LN to surrounding tissues 0.5–4 h post injection. *Ex vivo* examination revealed the popliteal LN noticeably swollen and emitted a much stronger probe signal (Fig. 5B). Bioluminescence imaging of the popliteal LN collected from tumor-bearing mice confirmed the presence of metastatic tumor cells (Fig. 5C). Owing to continuous infiltration of probes along the lymphatic vessels, rapid lymphatic imaging and gradual diffusion of fluorescent signals, failed leading to a high background signal with additional false-positive results in sciatic LNs detection. However, no obvious fluorescence signal or probe

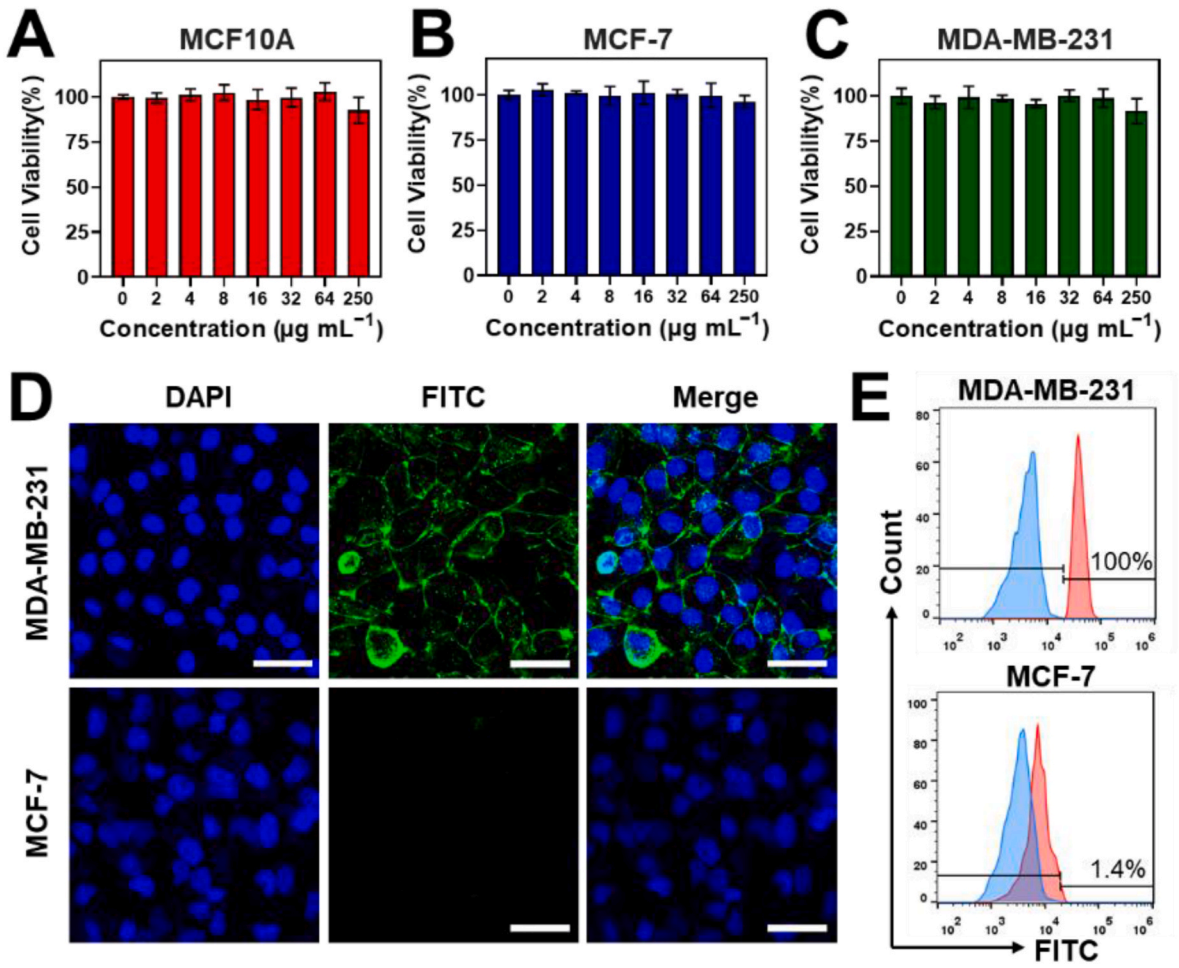


**Fig. 3.** Cytotoxicity and uptake of RENPs@HA *in vitro*. (**A–C**) Viability of MCF10A (**A**), MCF-7 (**B**), and MDA-MB-231 (**C**) cells incubated with RENPs@HA. (**D**) CLSM and (**E**) FCM of MCF-7 and MDA-MB-231 cells incubated with 200 μg $mL^{-1}$ RENPs@HA-FITC for 4 h, scale bar 50 μm. Data are expressed as the mean ± SD (n = 3).

penetration was observed in the inguinal lymph nodes throughout. This result means that probe drainage via the lymphatics could not provide accurate LNs detection, let alone specific diseased LNs screening, as complex and potentially pathological lymphatic drainage may increase the risk of false-negative detection [26,27].

Then, we investigated the ability of RENP@HA to provide long-term, specific imaging of diseased lymph nodes through intravenous administration. The same LNs metastasis model was imaged after intravenous injection of RENPs@HA (1 mg $kg^{-1}$), as shown in Fig. 5D. NIR-II fluorescence signals were observed in the popliteal LN in 1 h post intravenous injection and maintained an adequate SNR for 6 h (Fig. 5E), suggesting the target enrichment of the probes in LNs metastasis. The background fluorescence signal of pathological LN in the NIR-I and NIR-IIa regions was higher than that in the NIR-IIb region and appeared 4 h later. Furthermore, the SNR of the invaded popliteal LN compared to that of the contralateral normal popliteal LN was calculated (Fig. 5F). The SNR of NIR-IIb imaging of the metastatic lesion reached 9.24, which was 4–6 fold higher than the results of each other, effectively distinguishing lymphatic metastases. In addition, *ex vivo* fluorescence imaging of LNs confirmed the presence of the NIR-II NPs (Fig. 5G). All lesions and lymph nodes were pathologically verified by H&E staining, confirming the ability of RENP@HA to effectively distinguish diseased LNs.

Furthermore, we attempted to use this probe to diagnose spontaneous LN metastasis in 4T1-Luc subcutaneous tumor model. Mice were intravenously injected with RENP@HA (1 mg $kg^{-1}$) and imaged after 6 h. NIR-IIb fluorescence imaging demonstrated a bright signal in the LN located near the primary tumor (Fig. 6A), which was significantly higher than that in all organs except the liver and spleen both in *ex vivo* and *in vivo* fluorescence imaging (Fig. 6B and C), especially contrasts sharply with the normal sciatic nerve LN. Additionally, the distinct demarcation line observed between the tumor region and lymphoid tissue in the H&E-stained sections further confirmed the occurrence of metastasis to inguinal LN (Fig. 6D). These results provided evidence that the probe can target LN metastases for the diagnosis of spontaneous lymphatic metastasis.

### 3.6. *Visualization of minimal tumor sites using RENPs@HA in a peritoneal dissemination metastatic model*

Invasive breast carcinoma is prone to metastasis and dissemination, and is one of the most severe extra-abdominal tumors that causes peritoneal metastases in advanced-stage patients [28]. Peritoneal metastases are usually associated with a poor prognosis owing to the difficulty of detection in clinical practice [29,30], as the survival rate was significantly correlated with the resection rate of small residual lesions (less than 1 cm) [31,32]. Hence, the ability of RENPs@HA to detect breast tumors and peritoneal metastases in a peritoneal dissemination metastatic model and to guide resection using intraoperative fluorescence was investigated.

Peritoneal dissemination metastatic models were developed by intraperitoneal injection of 4T1-Luc cells (Fig. 7A). Then, the mice were intravenously injected with RENPs@HA (1 mg $kg^{-1}$) and imaged after 6 h (Fig. SI 5A). The NIR-II fluorescence signal of the multiple probe-

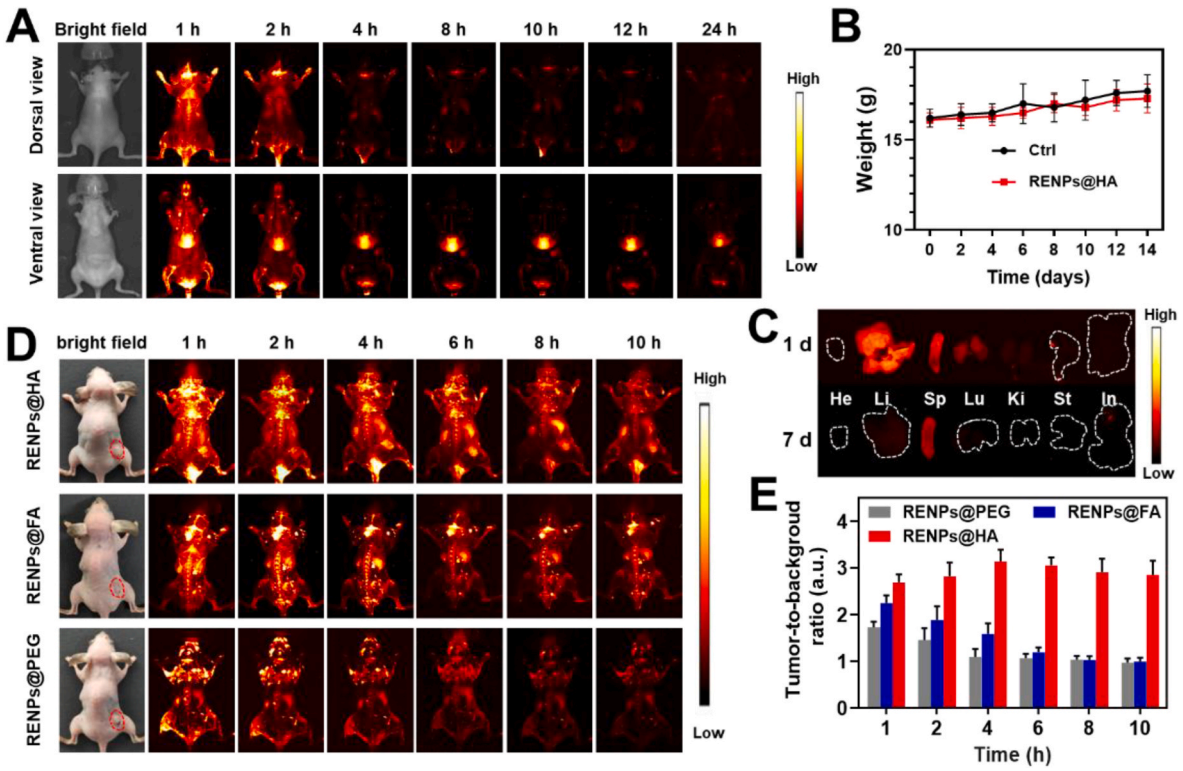


**Fig. 4.** Biodistribution and biocompatibility of RENPs@HA. (**A**) *In vivo* NIR-IIb fluorescence images of healthy mice with intravenous injection of RENPs@HA. (**B**) Body weight of mice over several days. (**C**) *Ex vivo* fluorescence images of the major organs (heart, liver, spleen, lungs, kidneys, stomach, and intestines) seven days post injection. (**D**) *In vivo* NIR-IIb fluorescence images of MDA-MB-231 tumor-bearing mice with intravenous injection of RENPs@HA, RENPs@FA and RENPs@PEG. (**E**) Quantitative analysis of tumor-to-background ratio of NIR-IIb fluorescence of the tumors in (**D**) using the ImageJ analysis software. Data are expressed as the mean ± SD (n = 3).

enriched regions could be detected by intraoperative imaging, and the SNR of 13.4 (n = 3) was observed to be nearly 3-fold higher than that of NIR-I imaging (Fig. SI 5B), thus avoiding false-positive signals from alimentary canal contents. Benefiting from the specific tumor-targeting ability of RENPs@HA, the signal of small metastatic lesions in the peritoneal metastasis model was accurately detected under conditions of liver signal exposure (without shelter) and was demonstrated by bioluminescence imaging (Fig. 7B and C; Fig. SI 5C). Thus, efficient NIR-IIb-guided complete resection of peritoneal metastases could be conducted with no residual minuscule tumors after surgery (Fig. SI 5D).

Additionally, the *in-situ* distribution of the probe in the removed tissue shown in fluorescence image was consistent with that exhibited by the *ex vivo* bioluminescence of malignant cells (Fig. 7D) with a sensitivity of 83.3 %, which could be peritoneal miliary disseminated lesions in the mesenteric LNs. Therefore, RENPs@HA was proved to accurately identify tumors at various miscellaneous locations and locate minuscule metastases during surgery.

## 4. Conclusion

Breast cancer guidelines require biopsies for preoperative assessment of all suspicious regional lymph nodes. However, the limitations of sampling techniques make it difficult to accurately detect and evaluate microscopic lesions smaller than 0.5 cm [33]. Prior research indicates that over 10 % of cases initially diagnosed as node-negative for breast cancer by blue dyes or radioactive nanocolloids actually contained micrometastases [34], defined by the American Joint Committee on Cancer as tumor deposits ranging from 0.2 to 2.0 mm in size [35]. This scenario further underscores the critical need for precise and immediate intraoperative detection of nodal metastasis.

NIR-II fluorescence imaging offers high-resolution imaging with minimal signal attenuation and high tissue penetration, which is highly advantageous for the real-time visualization of breast cancer lymph node metastases *in vivo*, both preoperatively and intraoperatively. Currently, ICG is the preferred NIR fluorescent small-molecule dye utilized in clinical settings as it rapidly migrates to the LNs within approximately 3 h [36]. Although ICG effectively identifies LNs, it cannot differentiate between metastatic and non-metastatic LNs. In this study, we effectively synthesized Er-based NIR-IIb rare earth nanoprobes RENPs@HA that exhibit characteristics such as deep tissue penetration, optical stability, and an imaging resolution of up to 41 μm using commercially available equipment. In contrast, the RENPs@HA nanoprobe was demonstrated the ability to accurately detect and persist in metastatic LNs for over 24 h.

The potential use of molecularly targeted probes to address metastatic diseases is of significant importance. Breast cancer cells exhibit increased expression of CD44 proteins, which is related to nodal metastases [18,37]. Additionally, lymphatic endothelial cells express a CD44 glycoprotein homologue lymphatic vessel endothelial hyaluronan receptor 1, which is a lymph-specific receptor with a specific affinity for HA [38,39]. Thus, HA is a screening marker and ideal candidate for designing novel metastasis targeting nanoprobes. In the present study, we conjugated RENPs with HA to create novel NIR-IIb fluorescent probes with superior tumor-targeting specificity for high SNR *in vivo* tumor imaging.

In addition, the complexity of lymphatic drainage pathways and the phenomenon of skipping lymphatic metastasis hinder the accuracy of LN diagnostics [40]. Even worse, the imaging efficacy of tracers through lymphatic drainage is significantly limited by sequential lymph node drainage patterns despite in regions of clear lymphatic drainage pathways [41]. Therefore, the intravenous administration of nanoprobes is more suitable for the visualization of early stage orthotopic microtumors and metastatic LNs. In this study, the intravenous administration of RENPs@HA effectively facilitated the visualization and detection of

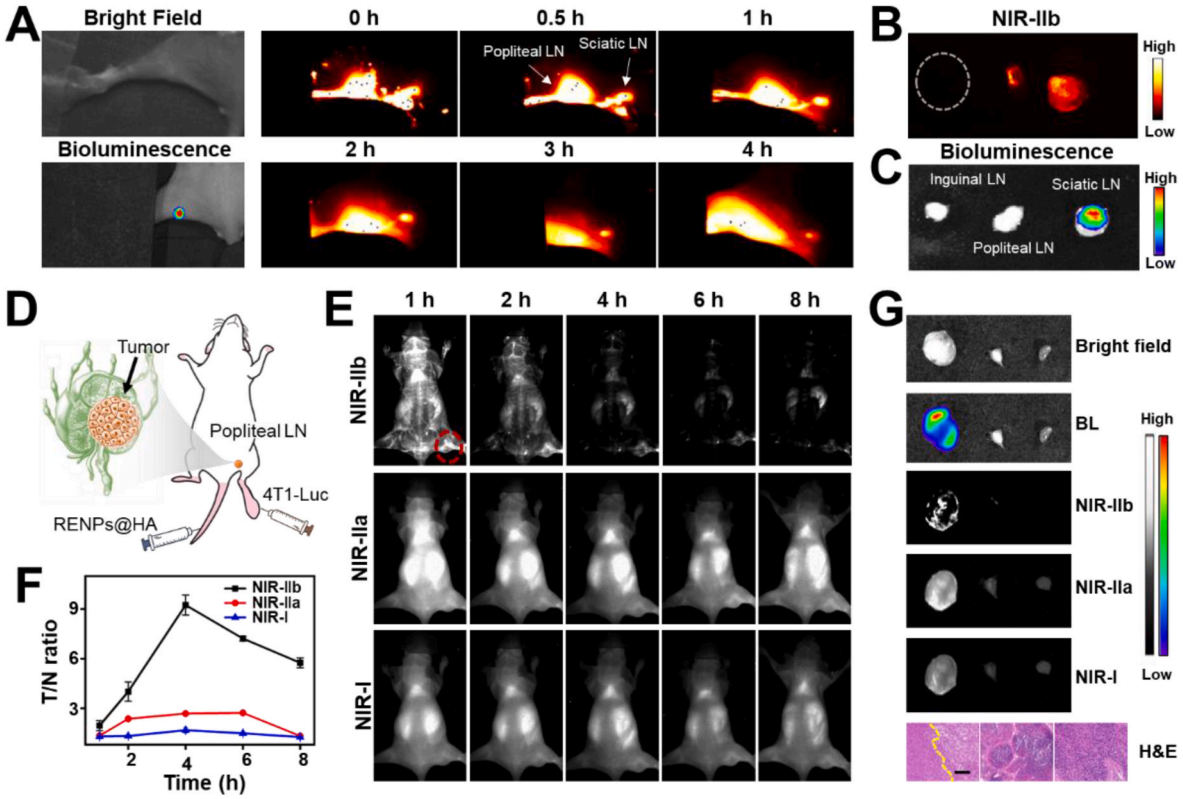


**Fig. 5.** *In vivo* NIR-IIb fluorescence imaging of SLNs with metastases. (**A**) *In vivo* imaging of mice with sciatic LN metastases after footpad injection of RENPs@HA. (**B**) NIR-IIb fluorescence imaging and (**C**) bioluminescence of sciatic LN, popliteal LN, and inguinal LN *ex vivo*. (**D**) Scheme of popliteal LN metastases detection through intravenous injection of RENPs@HA. (**E**) *In vivo* imaging of popliteal LN metastases after intravenous injection of RENPs@HA probe in NIR-I, NIR-IIa, and NIR-IIb regions. (**F**) SNR of SLN metastases in different imaging regions based on (**E**). (**G**) Bioluminescence, NIR fluorescence imaging, and H&E staining of popliteal LN, sciatic LN, and inguinal LN *ex vivo*. The yellow line in H&E staining shows the boundary between tumors and normal lymphoid tissue, scale bar 200 μm.

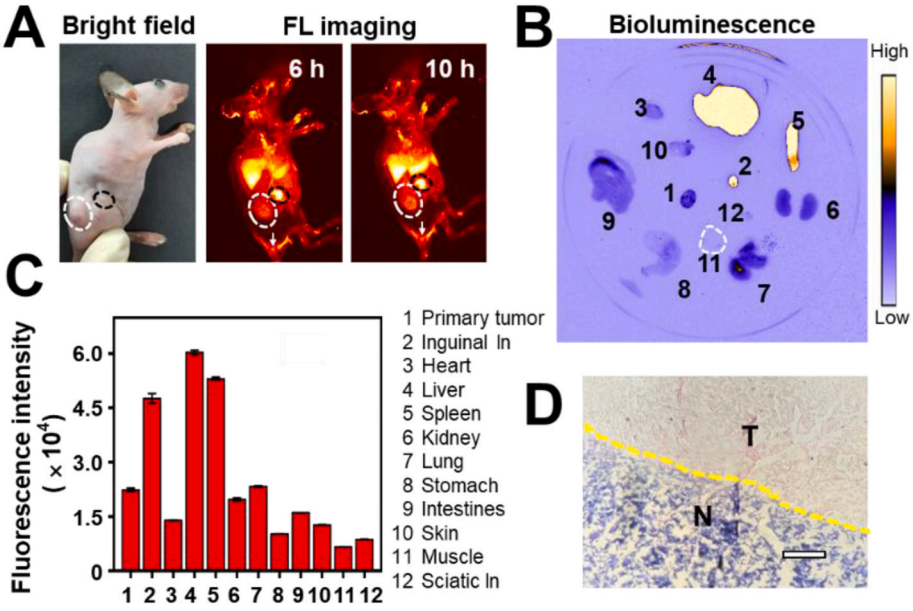


**Fig. 6.** Diagnosis of spontaneous lymph node metastasis. (**A**) *In vivo* NIR-IIb fluorescence images after intravenous injection of RENPs@HA. (**B**) *Ex vivo* fluorescence images of major organs and LNs 12 h post injection. (**C**) Quantitative analysis of NIR-IIb nanoprobe fluorescence intensity of various organs *ex vivo* based on (**B**). (**D**) H&E staining of pathological inguinal LN, scale bar 20 μm.

microtumors and abdominal LN metastases, leading to the guidance for surgical resection.

In summary, we developed an NIR-IIb rare earth nanoprobe, RENPs@HA, for the real-time detection and resection of SLN metastasis in breast cancer, which accurately determined LN status with high sensitivity and specificity and enabled the detection of macro- or micrometastases with great sensitivity. This methodology holds promise for the precise visualization of lymph node metastasis, thereby

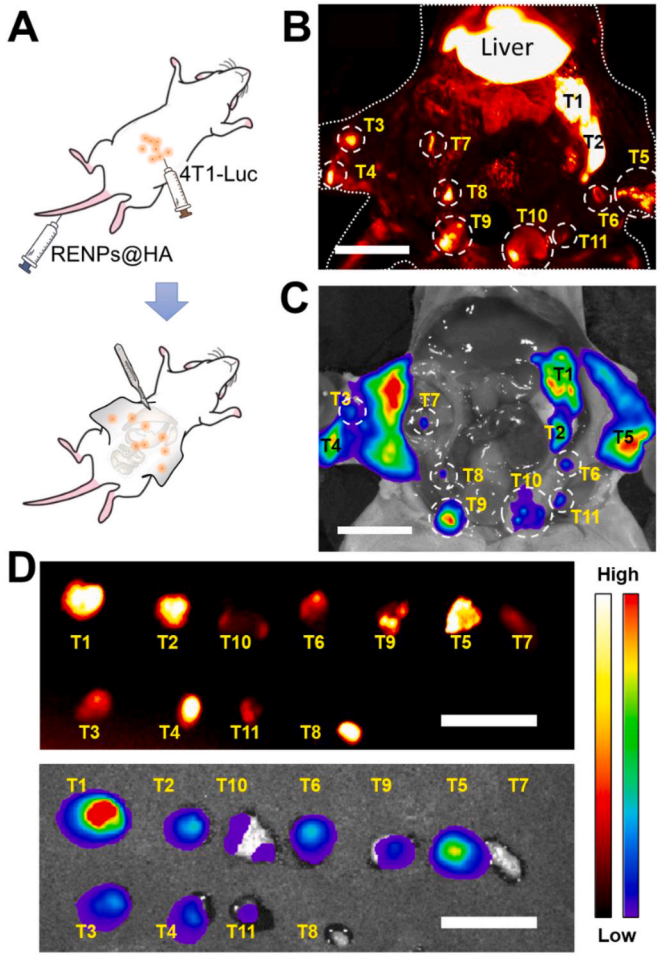


**Fig. 7.** Diagnosis and resection of minimal peritoneal dissemination metastasis. (**A**) Scheme of peritoneal dissemination for metastatic model establishment and surgical navigation. (**B**) *In vivo* NIR-IIb fluorescence images 4h post intravenous injection of RENPs@HA, scale bar 10 mm. (**C**) Bioluminescence imaging of peritoneal dissemination metastasis, scale bar 10 mm. (**D**) NIR-IIb fluorescence and bioluminescence imaging of minimal metastatic lesions *ex vivo* after fluorescence-guided surgery, scale bar 10 mm.

enhancing the advantages of early tumor staging and treatment decision-making.

## CRediT authorship contribution statement

**Zuo Yang:** Writing – original draft, Methodology, Data curation. **Yu Ji:** Methodology, Investigation, Formal analysis. **Qian Jia:** Writing – original draft, Validation, Investigation, Funding acquisition, Data curation. **Yanbin Feng:** Resources, Investigation. **Renchuan Ji:** Investigation, Data curation. **Mingli Bai:** Resources, Investigation. **Haohao Yan:** Resources, Investigation. **Fang Sun:** Resources, Investigation. **Ruili Zhang:** Writing – review & editing, Project administration, Conceptualization. **Zhongliang Wang:** Writing – original draft, Project administration, Funding acquisition, Conceptualization.

## Declaration of competing interest

The authors declare that they have no known competing financial interests or personal relationships that could have appeared to influence the work reported in this paper.

## Data availability

Data will be made available on request.

## Acknowledgements

This work was funded by the National Key Research and Development Program of China (No. 2022YFB3203800), National Natural Science Foundation of China (No. 82272159), China Postdoctoral Science Foundation (No. 2022TQ0249), the Hong Kong Scholars Program (No. XJ2023032), the Natural Science Basic Research Program of Shaanxi (No. 2024JC-YBQN-0111), the Postdoctoral Research Project of Shaanxi Province (No. 2023BSHEDZZ155), Innovation Capability Support Program of Shaanxi (No. 2022TD-52), Shaanxi Fundamental Science Research Project for Chemistry and Biology (Grant No. 23JHZ005), Guangdong Basic and Applied Basic Research Foundation (No. 2023A1515110803), Key Research and Development Program of Shaanxi (No. 2024SF-YBXM-126), the Fundamental Research Funds for the Central Universities (Nos. QTZX22068, XJSJ23189). This work was also funded by Xidian University.

## Appendix A. Supplementary data

Supplementary data to this article can be found online at https://doi.org/10.1016/j.mtbio.2024.101166.

## References

[1] H. Bois, T.A. Heim, A.W. Lund, Tumor-draining lymph nodes: at the crossroads of metastasis and immunity, Sci. Immunol. 6 (63) (2021) eabg3551.
[2] Y. Shou, S.C. Johnson, Y.J. Quek, X.L. Li, A. Tay, Integrative lymph node-mimicking models created with biomaterials and computational tools to study the immune system, Mater. Today Bio 14 (2022) 100269.
[3] G.H. Lyman, A.E. Giuliano, M.R. Somerfield, A.B. Benson, D.C. Bodurka, H. J. Burstein, A.J. Cochran, H.S. Cody, S.B. Edge, S. Galper, J.A. Hayman, T.Y. Kim, C.L. Perkins, D.A. Podoloff, V.H. Sivasubramaniam, R.R. Turner, R. Wahl, D. L. Weaver, A.C. Wolff, E.P. Winer, American society of clinical oncology guideline recommendations for sentinel lymph node biopsy in early-stage breast cancer, J. Clin. Oncol. 23 (30) (2005) 7703–7720.
[4] H. Verry, S.J. Lord, A. Martin, G. Gill, C.K. Lee, K. Howard, N. Wetzig, J. Simes, Effectiveness and cost-effectiveness of sentinel lymph node biopsy compared with axillary node dissection in patients with early-stage breast cancer: a decision model analysis, Br. J. Cancer 106 (6) (2012) 1045–1052.
[5] S. Vrande, J. Meijer, A. Rijnders, J.H.G. Klinkenbijl, The value of intraoperative frozen section examination of sentinel lymph nodes in breast cancer, Eur. J. Surg. Onc. 35 (3) (2009) 276–280.
[6] M. Ahmed, A.D. Purushotham, M. Douek, Novel techniques for sentinel lymph node biopsy in breast cancer: a systematic review, Lancet Oncol. 15 (8) (2014) e351–e362.
[7] Y.Y. Zhu, L. Song, Y.Q. Zhang, W.L. Liu, W.L. Chen, W.L. Gao, L.X. Zhang, J. Z. Wang, Z.H. Ming, Y. Zhang, G.J. Zhang, Development of a rare earth nanoprobe enables in vivo real-time detection of sentinel lymph node metastasis of breast cancer using NIR-IIb imaging, Cancer Res. 83 (20) (2023) 3428–3441.
[8] S.J. Zhu, B.C. Yung, S. Chandra, G. Niu, A.L. Antaris, X.Y. Chen, Near-infrared-II (NIR-II) bioimaging via off-peak NIR-I fluorescence emission, Theranostics 8 (15) (2018) 4141–4151.
[9] C.L. Tian, X. Sun, B.B. Cong, P.F. Qiu, Y.S. Wang, Murine model study of a new receptor-targeted tracer for sentinel lymph node in breast cancer, J. Breast Cancer 22 (2) (2019) 274–284.
[10] Y. Qian, H.L. Jin, S. Qiao, Y.F. Dai, C. Huang, L.S. Lu, Q.M. Luo, Z.H. Zhang, Targeting dendritic cells in lymph node with an antigen peptide-based nanovaccine for cancer immunotherapy, Biomaterials 98 (2016) 171–183.
[11] M. Hegde, N. Naliyadhara, J. Unnikrishnan, M.S. Alqahtani, M. Abbas, S. Girisa, G. Sethi, A.B. Kunnumakkara, Nanoparticles in the diagnosis and treatment of cancer metastases: current and future perspectives, Cancer Lett. 556 (2023) 216066.
[12] S. Karaman, M. Detmar, Mechanisms of lymphatic metastasis, J. Clin. Invest. 124 (3) (2014) 922–928.
[13] G.S. Hong, A.L. Antaris, H.J. Dai, Near-infrared fluorophores for biomedical imaging, Nat. Biomed. Eng. 1 (2017) 10.
[14] S.J. Zhu, R. Tian, A.L. Antaris, X.Y. Chen, H.J. Dai, Near-Infrared-II molecular dyes for cancer imaging and surgery, Adv. Mater. 31 (24) (2019) e1900321.
[15] J.W. Bai, S.Q. Qiu, G.J. Zhang, Molecular and functional imaging in cancer-targeted therapy: current applications and future directions, Sig. Transduct. Target. Ther. 8 (2023) 89.

[16] P.Y. Du, Y. Wei, Y. Liang, R. An, S.Y. Liu, P.P. Lei, H.J. Zhang, Near-infrared-responsive rare earth nanoparticles for optical imaging and wireless phototherapy, Adv. Sci. 11 (8) (2023) e1900321.
[17] Q. Jia, Z. Li, M.L. Bai, H.H. Yan, R.L. Zhang, Y. Ji, Y.B. Feng, Z. Yang, Z.L. Wang, J. X. Li, Estimating dynamic vascular perfusion based on Er-based lanthanide nanoprobes with enhanced down-conversion emission beyond 1500 nm, Theranostics 11 (20) (2021) 9859–9872.
[18] G. Nabil, R. Alzhrani, H.O. Alsaab, M. Atef, S. Sau, A.K. Iyer, H.E.l. Banna, CD44 targeted nanomaterials for treatment of triple-negative breast cancer, Cancers 13 (4) (2021) 898.
[19] Z.Q. Sun, H.Y. Huang, R. Zhang, X.H. Yang, H.C. Yang, C.Y. Li, Y.J. Zhang, Q. B. Wang, Activatable rare earth near-infrared-II fluorescence ratiometric nanoprobes, Nano Lett. 21 (15) (2021) 6576–6583.
[20] S.W. Kim, J.P. Zimmer, S. Ohnishi, J.B. Tracy, J.V. Frangioni, M.G. Bawendi, Engineering InAsxP1-x/InP/ZnSe III-V alloyed core/shell quantum dots for the near infrared, J. Am. Chem. Soc. 127 (30) (2005) 10526–10532.
[21] S. Kang, S. Ahn, J. Le, J.Y. Kim, M. Choi, V. Gujrati, H. Kim, J. Kim, E.C. Shin, S. Y. Jon, Effects of gold nanoparticle-based vaccine size on lymph node delivery and cytotoxic T-lymphocyte responses, J. Control. Release 256 (2017) 56–67.
[22] Z.F. Zhao, L.D. Wang, G. Zhan, Z.W. Liu, Z.Q. Bian, C.H. Huang, Efficient rare earth cerium(III) complex with nanosecond d-f emission for blue organic light-emitting diodes, Natl. Sci. Rev. 8 (2) (2021) nwaa193.
[23] F.F. Meng, J.P. Wang, Q.N. Ping, Y. Yeo, Quantitative assessment of nanoparticle biodistribution by fluorescence imaging, revisited, ACS Nano 12 (7) (2018) 6458–6468.
[24] J. Fang, W. Islam, H. Maeda, Exploiting the dynamics of the EPR effect and strategies to improve the therapeutic effects of nanomedicines by using EPR effect enhancers, Adv. Drug Deliv. Rev. 157 (2020) 142–160.
[25] J.Y. Lee, U. Termsarasab, J.H. Park, S.Y. Lee, S.H. Ko, J.S. Shim, S.J. Chung, H. J. Cho, D.D. Kim, Dual CD44 and folate receptor-targeted nanoparticles for cancer diagnosis and anticancer drug delivery, J. Control. Release 236 (2016) 38–46.
[26] S.D. Nathanson, M. Mahan, Sentinel lymph node pressure in breast cancer, Ann. Surg Oncol. 18 (3) (2011) 3791–3796.
[27] K.S. Blum, S.T. Proulx, P. Luciani, J.C. Leroux, M. Detmar, Dynamics of lymphatic regeneration and flow patterns after lymph node dissection, Breast Cancer Res. Treat. 139 (1) (2013) 81–86.
[28] M. Tuthill, R. Pell, R. Guiliani, A. Lim, M. Gudi, K.B. Contractor, J.S. Lewis, R. C. Coombes, J. Stebbing, Peritoneal disease in breast cancer: a specific entity with an extremely poor prognosis, Eur. J. Cancer 45 (12) (2009) 2146–2149.
[29] M. Miyazaki, A. Nakabo, Y. Nagano, Y. Nagamura, K. Yanagihara, R. Ohki, Y. Nakamura, K. Fukami, J. Kawamoto, K. Umayahara, M. Sakamoto, K. Iwaya, H. Yamaguchi, Tissue factor-induced fibrinogenesis mediates cancer cell clustering and multiclonal peritoneal metastasis, Cancer Lett. 553 (2023) 215983.
[30] V. Kepenekian, A. Bhatt, J. Péron, M. Alyami, N. Benzerdjeb, N. Bakrin, C. Falandry, G. Passot, P. Rousset, O. Glehen, Advances in the management of peritoneal malignancies, Nat. Rev. Clin. Oncol. 19 (11) (2022) 698–718.
[31] P. Harter, J. Sehouli, I. Vergote, G. Ferron, A. Reuss, W. Meier, S. Greggi, B. J. Mosgaard, F. Selle, F. Guyon, C. Pomel, F. Lécuru, R. Zang, E.A. Lundqvist, J. W. Kim, J. Ponce, F. Raspagliesi, G. Kristensen, J.M. Classe, P. Hillemanns, P. Jensen, A. Hasenburg, S.G. Maghami, M.R. Mirza, B. Lund, A. Reinthaller, A. Santaballa, A. Olaitan, F. Hilpert, A.D. Bois, Randomized trial of cytoreductive surgery for relapsed ovarian cancer, N. Engl. J. Med. 385 (23) (2021) 2123–2131.
[32] R.A. Mukhtar, C. Yau, L.J. Esserman, Prognostic significance of residual ductal carcinoma in situ after complete response of invasive breast cancer to neoadjuvant therapy reply, JAMA Surg 158 (6) (2023) 675.
[33] S.X. Sun, T.W. Moseley, H.M. Kuerer, W.T. Yang, Imaging-based approach to axillary lymph node staging and sentinel lymph node biopsy in patients with breast cancer, Am. J. Roentgenol. 214 (2) (2020) 249–258.
[34] D. Park, R. Kåresen, B. Naume, M. Synnestvedt, E. Beraki, T. Sauer, The prognostic impact of occult nodal metastasis in early breast carcinoma, Breast Cancer Res. Treat. 118 (1) (2009) 57–66.
[35] A.B. Olawaiye, T.P. Baker, M.K. Washington, D.G. Mutch, The new (Version 9) American Joint Committee on Cancer tumor, node, metastasis staging for cervical cancer, CA Cancer J. Clin. 71 (4) (2021) 287–298.
[36] J.S.D. Mieog, F.B. Achterberg, A. Zlitni, M. Hutteman, J. Burggraaf, R. J. Swijnenburg, S. Gioux, A.L. Vahrmeijer, Fundamentals and developments in fluorescence-guided cancer surgery, Nat. Rev. Clin. Oncol. 19 (1) (2022) 9–22.
[37] M. Götte, G.W. Yip, Heparanase, hyaluronan, and CD44 in cancers: a breast carcinoma perspective, Cancer Res. 66 (21) (2006) 10233–10237.
[38] L.A. Johnson, S. Banerji, W. Lawrance, U. Gileadi, G. Prota, K.A. Holder, Y. M. Roshorm, T. Hanke, V. Cerundolo, N.W. Gale, D.G. Jackson, Dendritic cells enter lymph vessels by hyaluronan-mediated docking to the endothelial receptor LYVE-1, Nat. Immunol. 18 (7) (2017) 762.
[39] Q.S. Wang, R. He, F. Yang, L.J. Kang, X.Q. Li, L. Fu, B. Sun, Y.M. Feng, FOXF2 deficiency permits basal-like breast cancer cells to form lymphangiogenic mimicry by enhancing the response of VEGF-C/VEGFR3 signaling pathway, Cancer Lett. 420 (2018) 116–126.
[40] H.L. Chung, J. Sun, J.W.T. Leung, Breast cancer skip metastases: frequency, associated tumor characteristics, and role of staging nodal ultrasound in detection, Am. J. Roentgenol. 217 (4) (2021) 835–843.
[41] G. Munbauhal, T. Seisen, F.D. Gomez, B. Peyronnet, O. Cussenot, S.F. Shariat, M. Rouprêt, Current perspectives of sentinel lymph node dissection at the time of radical surgery for prostate cancer, Cancer Treat Rev. 50 (2016) 228–239.